ACS NANO

www.acsnano.org

ARTICLE

Self-Assembly of Ionic Superdiscs in Nanopores

Zhuoqing Li, Aileen Raab, Mohamed Aejaz Kolmangadi, Mark Busch, Marco Grunwald, Felix Demel, Florian Bertram, Andriy V. Kityk, Andreas Schönhals, Sabine Laschat, and Patrick Huber*

Cite This: https://doi.org/10.1021/acsnano.4c01062

Read Online

ACCESS | Metrics & More | Article Recommendations | Supporting Information

ABSTRACT: Discotic ionic liquid crystals (DILCs) consist of self-assembled superdiscs of cations and anions that spontaneously stack in linear columns with high one-dimensional ionic and electronic charge mobility, making them prominent model systems for functional soft matter. Compared to classical nonionic discotic liquid crystals, many liquid crystalline structures with a combination of electronic and ionic conductivity have been reported, which are of interest for separation membranes, artificial ion/proton conducting membranes, and optoelectronics. Unfortunately, a homogeneous alignment of the DILCs on the macroscale is often not achievable, which significantly limits the applicability of DILCs. Infiltration into nanoporous solid scaffolds can, in principle, overcome this drawback. However, due to the experimental challenges to scrutinize liquid crystalline order in extreme spatial confinement, little is known about the structures of DILCs in nanopores. Here, we present temperature-dependent high-resolution optical birefringence measurement and 3D reciprocal space mapping based on synchrotron X-ray scattering to investigate the thermotropic phase behavior of dopamine-based ionic liquid crystals confined in cylindrical channels of 180 nm diameter in macroscopic anodic aluminum oxide membranes. As a function of the membranes' hydrophilicity and thus the molecular anchoring to the pore walls (edge-on or face-on) and the variation of the hydrophilic−hydrophobic balance between the aromatic cores and the alkyl side chain motifs of the superdiscs by tailored chemical synthesis, we find a particularly rich phase behavior, which is not present in the bulk state. It is governed by a complex interplay of liquid crystalline elastic energies (bending and splay deformations), polar interactions, and pure geometric confinement and includes textural transitions between radial and axial alignment of the columns with respect to the long nanochannel axis. Furthermore, confinement-induced continuous order formation is observed in contrast to discontinuous first-order phase transitions, which can be quantitatively described by Landau-de Gennes free energy models for liquid crystalline order transitions in confinement. Our observations suggest that the infiltration of DILCs into nanoporous solids allows tailoring their nanoscale texture and ion channel formation and thus their electrical and optical functionalities over an even wider range than in the bulk state in a homogeneous manner on the centimeter scale as controlled by the monolithic nanoporous scaffolds.

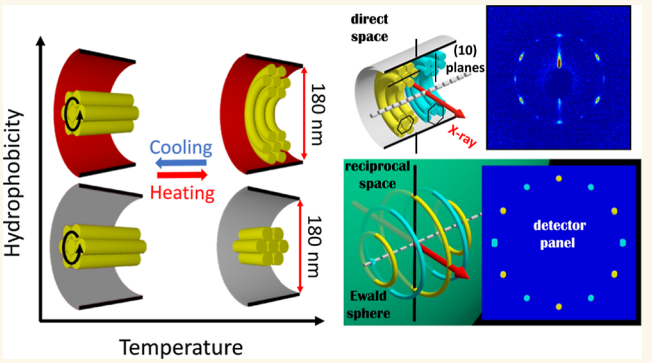

KEYWORDS: *ionic liquid crystal, nanoporous material, Landau de-Gennes analysis, X-ray scattering, optical birefringence*

INTRODUCTION

Ionic liquid crystals (ILCs) are salts composed of large organic cations and anions.[1,2] They bridge the gap between conventional ionic liquids and liquid crystals (LCs) and show great potential in fundamental physicochemical research.[1,3] Compared to conventional ionic liquids, ILCs often possess long alkyl chains and various functional groups that allow the tailoring of their molecular structure and the corresponding self-assembled mesophases.[4] Among the various ILCs, those with a discotic structure have attracted particular interest. Discotic ionic liquid crystals (DILCs) often contain aromatic cores in their large cation units. Driven by the $\pi-\pi$ interaction and electrostatic interaction between the aromatic cores, DILCs may self-organize and stack up in columns, resulting

Received: January 23, 2024
Revised: April 23, 2024
Accepted: May 1, 2024

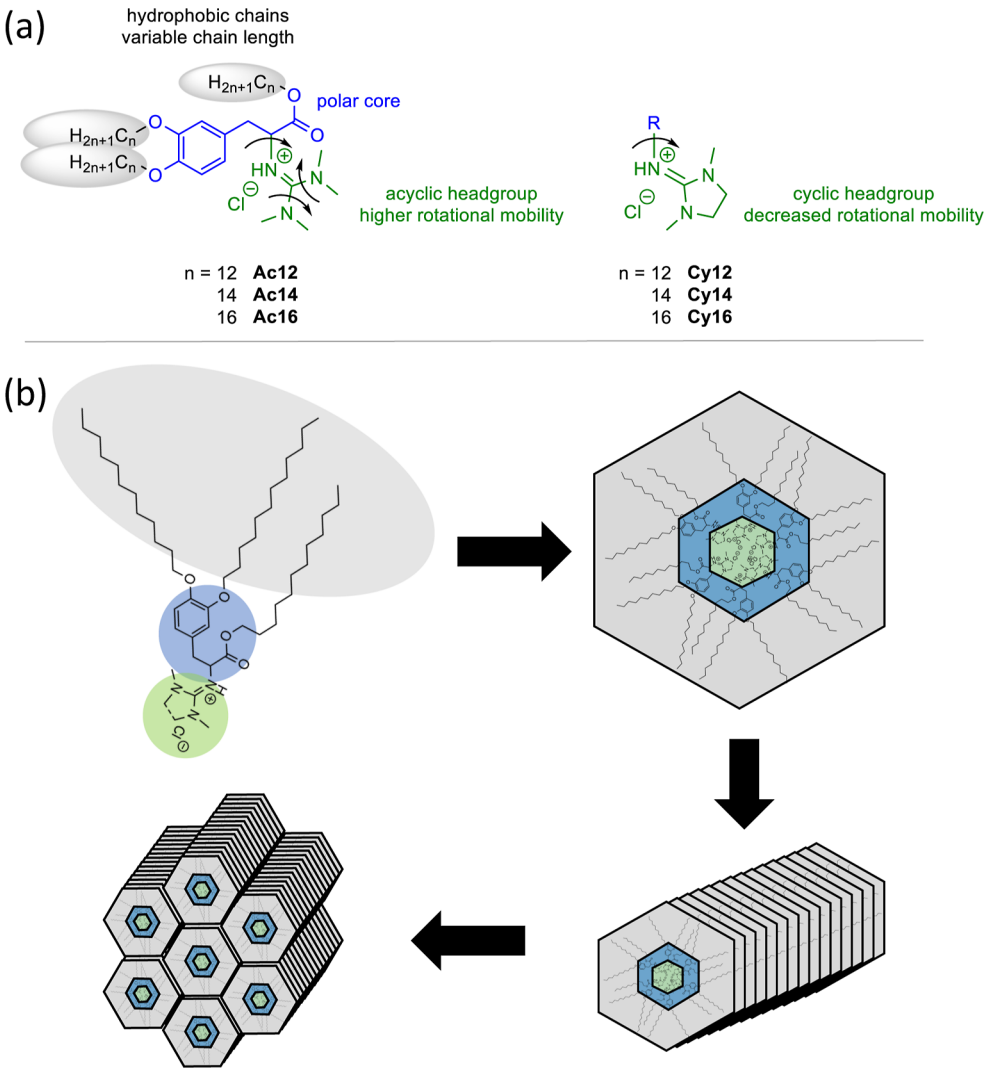

Figure 1. Multiscale self-assembly of a columnar DILC. (a) Chemical formula of a single ILC molecular block based on L-3,4-dihydroxyphenylalanine (Dopa-ILC), consisting of a hydrophilic aromatic core (blue), an ion group (green), and three hydrophobic alkyl chains of different lengths (gray). An acyclic (left) or cyclic (right) five-membered imidazolium ring is attached as a functional group to the core. (b) Schematic of six Dopa-ILC molecules self-assembling into a superdisc (discotic unit) with a hydrophilic inner core and surrounding hydrophobic alkyl chains. Calculated from the X-ray diffraction results, the typical size of a superdisc composed of six acyclic Dopa-ILC molecules with a side chain of 12 carbon atoms is 6.85 nm.[10] Due to the $\pi-\pi$ interaction between the discs, the discotic units can stack up to form a column. The columns can self-organize further to form a hexagonal columnar liquid crystalline mesophase.

in a hexagonal ordered columnar liquid crystalline mesophase; see Figure 1.[5] The overlapping π electrons also provide high one-dimensional charge carrier mobility along the columnar axes often leading to semiconducting properties.[6,7] DILCs therefore combine the high ionic diffusion and conductivity of ionic liquids with the self-assembly and stimulus-responsive anisotropy of conventional discotic liquid crystals (DLCs).[8] The unique properties of DILCs allow the design of stimuli-responsive conductors for energy storage devices, electrochromic supercapacitors, flexible batteries, separation media, and optoelectronic devices.[9] In particular, the stimuli-responsive phase transition of DILCs allows the direction of ionic conduction to be modulated.[2]

Over the past two decades, many successful attempts have been made on the self-alignment of conventional DLCs. Kawata demonstrates the successful establishment of hybrid, horizontal, vertical, and vertical-twisted alignments of DLCs on web-coating thin films, utilizing materials including photo-polymerizable DLCs, alignment promoters, alignment layers, and chiral agents, leading to enhanced viewing angles in thin film transistor liquid crystal displays.[11] Eichhorn et al. reviewed the diverse methods including mechanical, magnetic, and solvent-induced techniques for aligning bulk materials of DLCs.[12] Lugger et al. have developed a method utilizing polymerizable hexagonal columnar DLCs to create nanostructured polymer films with continuous, membrane-spanning pores, demonstrating enhanced adsorption capabilities.[13] Pipertzis et al. have shown that doping DLCs with salts at different ratios enables the conduction of both electronic charge and ions on nanometer length scales. A combination of ionic conductivity and mechanical stability makes them potential electrolytes.[14] Based on the study on conventional DLCs, a large number of synthesis strategies of DILCs have also been established and the properties of DILCs have been studied experimentally and theoretically.[1,4,15] Unfortunately, a homogeneous alignment of the DILCs on the macroscale is

https://doi.org/10.1021/acsnano.4c01062
ACS Nano XXXX, XXX, XXX−XXX

often not achievable, which significantly limits their applicability. One possible reason for this is that electric field-induced orientation, which is a commonly used orientation method for typical LCs, is not applicable to ILCs due to their ionic nature.[9] Infiltration into interface-dominated nanoporous solid scaffolds can overcome this shortcoming, as has been demonstrated for many other soft matter systems, most notably nonionic liquid crystalline materials.[16−24]

However, because of spatial and topological constraints, the phase and self-assembly behavior of confined soft matter[25−29] and in particular confined LCs may substantially deviate from the bulk state and DILCs have been little studied in that respect so far.[16,23,30−45]

Several previous studies have been performed on conventional, nonionic DLCs under nanoconfinement, especially in cylindrical pores of nanoporous anodic aluminum oxide (AAO) templates.[6,23,46−54] As a basis for the discussion of our results, we present the peculiar textures found in these studies. As shown in Figure 2, due to the hydrophilicity of the

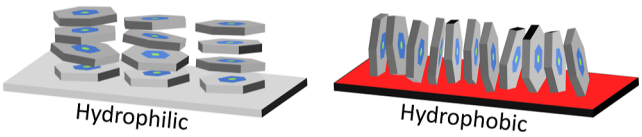

Figure 2. Anchoring of DILCs at planar surfaces. (a) Face-on (homeotropic) anchoring and (b) edge-on (planar or homogeneous) anchoring of DILC molecules on a hydrophilic and hydrophobic surface, respectively.

aromatic core of the discs and the hydrophobicity at the disc edges, DLC molecules often adopt face-on (homeotropic) anchoring on hydrophilic flat surfaces and edge-on (planar or homogeneous) anchoring on hydrophobic flat surfaces.

What liquid crystalline textures result from these different anchorings depending on the pore wall hydrophilicity in the cylindrical channels of AAO? For as-prepared AAO with its polar, hydrophilic pore walls, either radial disc arrangements as shown in Figure 3a[49] or the so-called logpile structures have

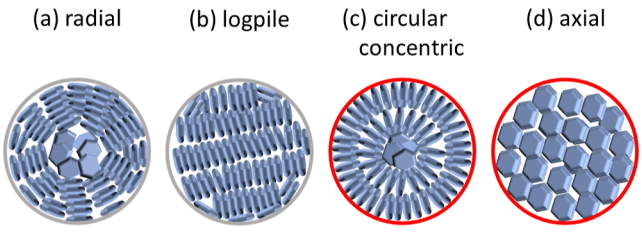

Figure 3. Top view of columnar discotic liquid-crystalline order in cylindrical nanopores. (a) Radial and (b) logpile configurations are typical for face-on anchoring at hydrophilic pore walls and (c) circular concentric and (d) axial configurations are typical for edge-on anchoring at hydrophobic pore walls.[6,23,49,50]

been deduced, see Figure 3b.[50,51] The latter are characterized by mostly straight and parallel columns arranged in layers perpendicular to the cylindrical pore axis. Since the stacking orientation can vary along the channel, the texture is reminiscent of logs in an ordered pile. Only near the pore wall do the columns splay slightly.

In terms of electrical conductivity and thus the suitability for molecular wires, neither configuration is preferred because no percolating conduction paths are established along the cylindrical channel. One might think that hydrophobic anchoring should solve this problem, since an axial alignment of the columns and thus nicely aligned conduction paths along the long axes of the AAO nanochannels should be the natural configuration fulfilling the edge-on anchoring condition at the pore wall. However, as shown by Zhang et al.[51] in reciprocal space mapping experiments and atomic force microscopy, DLCs often form circular concentric rings instead of straight columns aligned parallel to the long cylindrical AAO pore axes.

The main cause of these two peculiar liquid crystalline textures, "circular concentric" and "logpile" and thus the avoidance of an axial arrangement in cylindrical nanoconfinement, be it hydrophilic or hydrophobic, is the very high splay energy and low bending energy of the columnar phases.[51] In fact, it could be shown that the axial configuration can be induced by increasing the column bending energy, e.g., by choosing DLCs with large aromatic cores and thus increased column stiffness.[51] Another way of achieving the preferred axial arrangement is the selection of small pore sizes, since the elastic cost for the deformation of the hexagons at the pore walls which disfavors this arrangement compared to the circular concentric state decreases with pore size, so that eventually for hydrophobic channels also an axial arrangement prevails, even for DLCs with relatively small aromatic cores such as 2,3,6,7,10,11-hexakis(hexyloxy)triphenylene (HAT6).[6,23,51,53]

To what extent these peculiarities with regard to the formation of axially arranged columnar phases are also typical for DILCs confined in AAO is the main focus of the present study. In fact, some previous work has also been done on confined DILCs. Kolmangadi et al. used a combination of dielectric spectroscopy, calorimetry, and X-ray scattering to show that the isotropic-to-columnar discotic transition of a DILC appears to be continuous, despite a discontinuous first-order bulk phase transition.[55] However, a detailed understanding of the structure and texture formation of DILCs in confinement is still lacking.

Here, we investigate the temperature-dependent translational and collective orientational order of DILCs with varying alkyl side-chain lengths and thus varying hydrophilicity confined in cylindrical nanochannels of 180 nm diameter with different mesogen pore-wall anchoring (hydrophilic, face-on or hydrophobic, edge-on) by synchrotron-based X-ray scattering and high-resolution optical birefringence measurements. Moreover, the DILC has a cyclic or acyclic side group, respectively, where the cyclic group, in contrast to the acyclic one, exhibits a suppressed rotational motion. Thus, the acyclic one shows more rotational dynamics and could thus contribute more disordering effects compared to the cyclic one.[56,57]

RESULTS AND DISCUSSION

Translational and Collective Orientational Order of Cyclic Dopa-ILCs Confined in 180 nm AAO Membranes.

In Figure 4, we show the birefringence measurements and the small-angle X-ray scattering (SAXS) results of the Dopa-ILCs with cyclic imidazolium five-membered ring (cyclic Dopa-ILCs) confined in both hydrophilic (a−c) and hydrophobic (d−f) nanoporous AAO membranes with a pore size of 180 nm. The details about the hydrophilic and hydrophobic confinement are explained in the 'Materials' chapter.

We will start our discussion of the cyclic Dopa-ILC with the shortest side chain length n = 12 (Cy12). As shown in Figure 4a(i), the optical retardation increases as the sample cools

https://doi.org/10.1021/acsnano.4c01062
ACS Nano XXXX, XXX, XXX−XXX

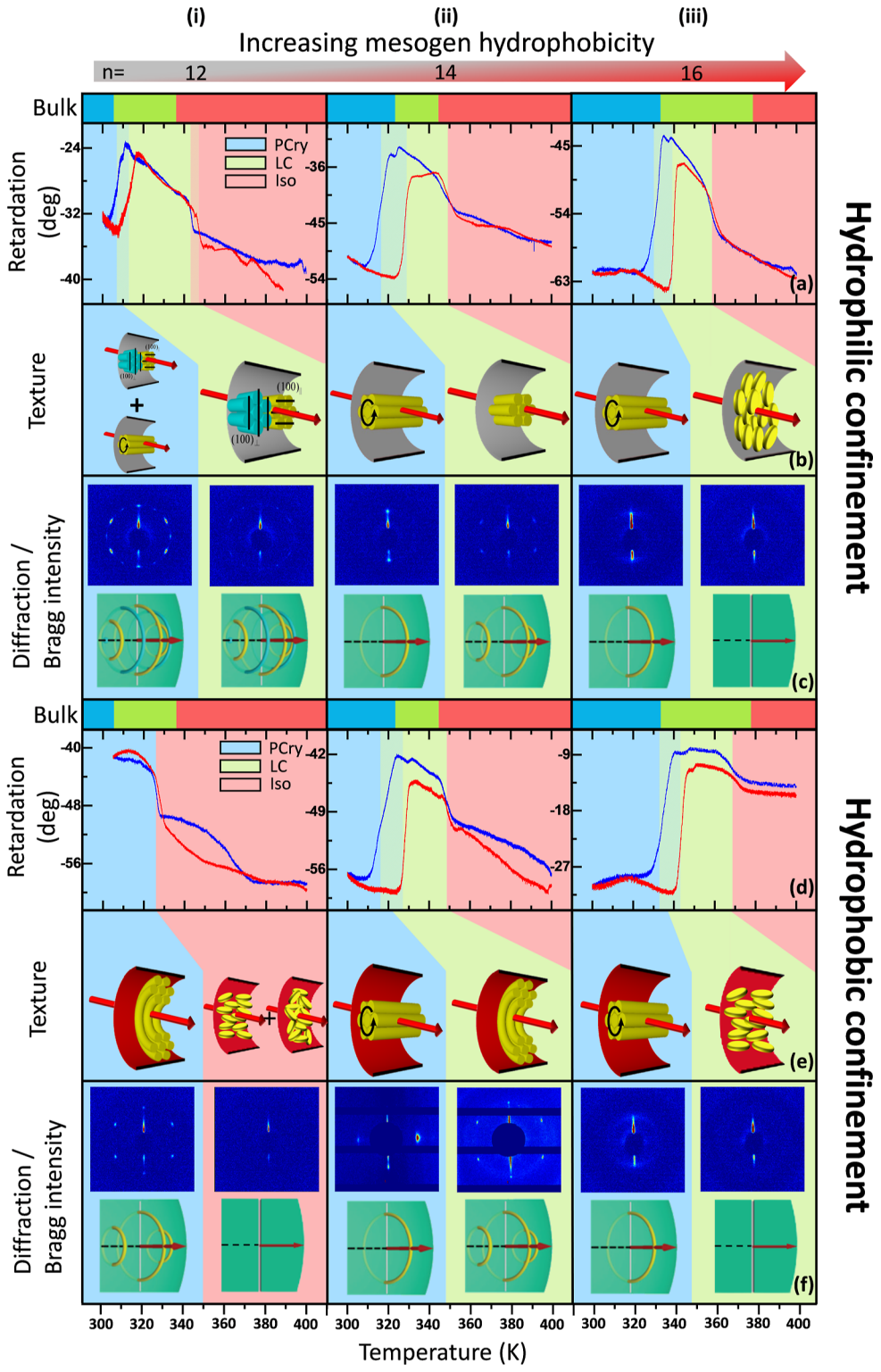

Figure 4. Self-assembly of cyclic Dopa-ILCs as a function of mesogen hydrophobicity in hydrophilic and hydrophobic nanochannels. Optical retardation and SAXS patterns of cyclic Dopa-ILC molecules with different side chain lengths n = 12 (i), 14 (ii), and 16 (iii) confined in hydrophilic (native) and hydrophobic (ODPA-modified) nanopores with 180 nm pore size. The temperature ranges of the distinct bulk phases of each Dopa-ILC are given above its retardation curve. The measured SAXS patterns and schematics of the corresponding scattering geometry and Bragg intensities in reciprocal space intersecting the Ewald sphere in both the plastic crystalline (PCry) and liquid crystalline (LC) phases are given. The background color refers to different phases of the DILCs under confinement (blue: PCry phase, green: LC phase, red: isotropic (Iso) phase). The dashed areas at the phase transition are the hysteresis between cooling and heating.

down with one relatively sharp increase at about 342 K. This indicates the formation of a collective orientational order where the superdiscs are aligned with their normal perpendicular to the long pore axis. Upon further cooling below 310 K, however, a decrease in the optical retardation indicates a full or at least partial reorientation of the superdiscs'

https://doi.org/10.1021/acsnano.4c01062
ACS Nano XXXX, XXX, XXX−XXX

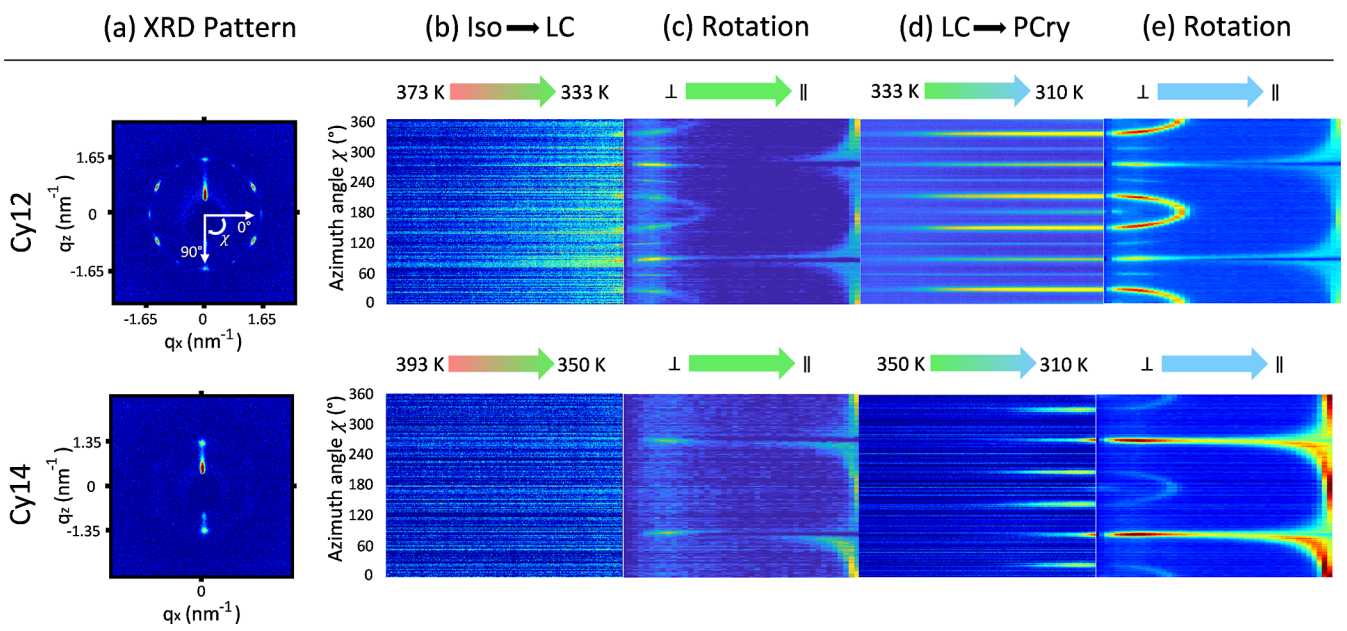

Figure 5. Texture evolution for Cy12 and Cy14 confined in hydrophilic nanochannels upon cooling to the LC and PCry phase. The upper and lower rows contain X-ray scattering data with regard to Cy12 and Cy14, respectively. (a) X-ray diffraction patterns at T = 310 K in the PCry phase. The peaks indicate the wave vector transfer $q_{(10)}$ characteristic of the hexagonal intercolumnar order. (b) Plotted is the color-coded scattering intensity at a fixed modulus of the wave vector transfer $q_{(10)}$ as a function of azimuth angle χ (vertical) for a fixed ω = 85° upon cooling from $T_{Iso\rightarrow LC}$, (c) in the LC phase upon rotation of the membrane from a perpendicular to a parallel orientation of the pore axis $\hat{p}$ with regard to the beam and (d,e) analogous scans upon cooling from $T_{LC\rightarrow PCry}$ and sample rotation in the PCry phase.

normals, parallel to the long cylindrical pore axes. Upon heating, this peculiar reorientational behavior is inverted, and again, two orientational ordering transitions are observed with small temperature hystereses of about 5 K between cooling and heating.

The X-ray diffraction experiment gives additional important information about the translational order of the superdiscs. Below 342 K, we observe a set of 12 diffraction peaks at a modulus of the wave vector transfer q typical of the (100) Bragg peak of hexagonal columnar order. It can be explained by the formation of two distinct domains of logpile structures where the columns grow in the radial direction, where however for the one domain the (100) lattice planes are perpendicular to the long pore axis, whereas they are parallel to the long pore axis for the second domain. Along with the rotation symmetry about the long cylindrical axis, this results in a set of green and yellow Bragg ring intensities in reciprocal space shown in Figure 4c(i). For our geometry and an incident beam perpendicular to the long channel axes, these rings intersect at 12 points with the Ewald sphere, resulting in the 12-fold diffraction pattern observed.

Figure 5 plots the Bragg peak intensities of Cy12 and Cy14 confined in 180 nm hydrophilic pores at each azimuth angle during cooling and rotational scans. When the samples are in the high-temperature Iso phase, their XRD patterns show no diffraction peaks from ILC structures, only membrane reflections at χ = 90 and 270°. To eliminate the membrane reflections, the membrane reflection SAXS peaks at the Iso phase are subtracted from all other temperatures. In Figure 5c, at the LC phase temperature, a rotational scan is performed where we can see a very weak 12-fold pattern in Cy12 and a pair of equatorial peaks in Cy14 as discussed above. Upon further cooling into the PCry phase, the 12-fold pattern of Cy12 becomes stronger in both the cooling scan of $T_{LC\rightarrow PCry}$ and the rotation scan in the PCry phase. Interestingly, from the Bragg intensity distribution, it can be seen that the peaks resulting from the (100)∥ domains (χ = 30, 90, 150, 210, 270, and 330°) are more prominent than the remaining peaks resulting from the (100) ⊥ domains, indicating that the (100) ∥ domains dominate in the pores over the (100) ⊥ domains. On the other hand, upon further cooling to the Cry phase, the equatorial peaks of Cy14 change to a hexagonal pattern at around 325 K, indicating the structural transformation from an axial structure to a logpile structure.

Thus, both our optical and X-ray experiments consistently indicate the formation of logpile structures upon cooling from the isotropic phase. Upon cooling below the second transition in the optical experiments, we see barely any change in the diffraction patterns, except for an increase in the intensity of the (100) ∥ domain. By contrast, the decrease in optical retardation hints at least at a partial axial orientation of the columns. Therefore, we infer a coexistence of axial and logpile columnar textures, see Figure 4b(i),c(i).

These findings are different from the observations for the more hydrophobic mesogens Cy14 and Cy16. For both systems, analogous to Cy12, we see first an increase in optical retardation and then a sharp drop. However, two Bragg peaks in equatorial directions (at χ = 90 and 270°) at positions typical of the intercolumnar distance are dominant at low T in the PCry phase. These equatorial peaks at low T can be explained by one ring in reciprocal space which results from a hexagonal columnar order along the long pore axis with randomization of the hexagonal orientation about the pore axis, see Figure 4b(ii),c(ii). Thus, we have evidence of axial order at low temperatures in the PCry phase for both mesogens. In the lower panels of Figure 5, these findings are documented in more detail by temperature- and rotation-dependent contour plots of the $q_{(10)}$ intensity for Cy14. We observe in the intermediate T-range (between the LC and the PCry phase, 350−330 K) only a 6-fold pattern typical of the

https://doi.org/10.1021/acsnano.4c01062
ACS Nano XXXX, XXX, XXX−XXX

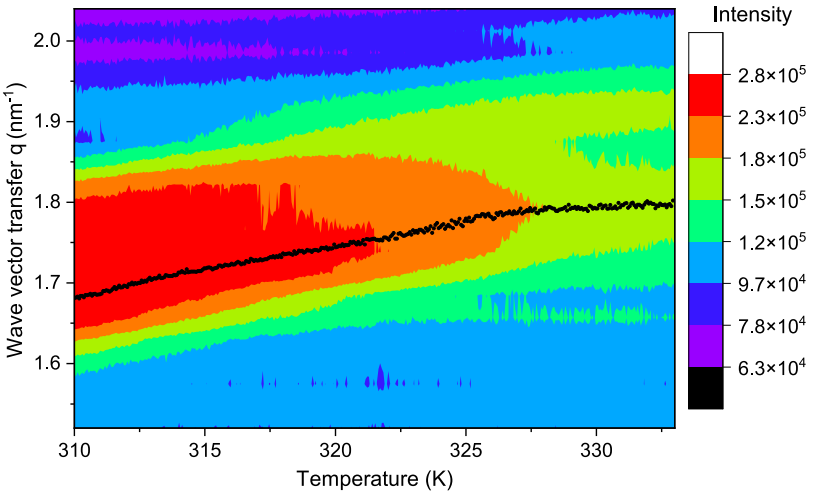

Figure 6. Negative thermal expansion of the intercolumnar lattice of Cy12 in 180 nm pores. Plotted is the color-coded X-ray scattering intensity as a function of temperature in the vicinity of the wave vector transfer of the dominating hexagonal (10) Bragg peak position $q_{(10)} = 4\pi/(\sqrt{3}\,d)$, where d is the intercolumnar lattice constant, as a function of temperature. As a guide for the eye, the position of the maximum intensity is indicated as a black line. It increases with increasing temperature indicating a Bragg peak shift to higher q with increasing temperature and thus an unconventional decreasing lattice parameter (negative thermal expansion).

(100) ∥ domain, with no coexistence with (100) ⊥ domains. Note that these scans reveal that additionally to the dominating axial peaks also scattering intensity emerges at positions typical of the logpile structure; see panel (d,e). Thus, also a presumably very small fraction of logpile textures is present in coexistence with the dominating axial arrangement.

Interestingly, for the Cy16 mesogen no translational order can be inferred at all in the LC phase, despite the increase in collective radial orientational order indicated by the polarimetry experiments; see Figure 4c(iii). Hence, the system forms a discotic nematic phase.

Overall, we find quite some analogies with classical discotic systems in terms of the formation of logpile structures with a preferred hexagonal axis orientation with regard to the long pore axis. Moreover, by increasing the hydrophobicity (chain length) of the mesogens, the systems show an increasing tendency to perform a textural transition from a logpile configuration to axial order. These textural transitions are consistent with LC to PCry transitions of the bulk and are therefore likely to be triggered by improved columnar rigidity. This could be caused by a gradual freezing (increasing all-trans configuration) of the alkyl side chains upon cooling. Such freezing effects of the alkyl side chains can be observed in many DLC systems when cooled from the LC phase to the crystalline phase. In this study, on slow cooling to the PCry phase, the three alkyl chains of Dopa-ILCs gradually lose their flexibility as the chain stiffness increases, resulting in increasing intercolumnar spacing. We exemplify this behavior in Figure 6 for Cy12 in hydrophilic pores. Note that the overall improved hexagonal columnar order is also evidenced by the increase in the $q_{(10)}$ peak intensities in the PCry phase. For other discotic systems, changes in the tilt angle of the discs with respect to the columnar axis have been found upon entry into the crystalline phase.[58] This can also lead to a negative thermal expansion. Since we do not see any evidence for such an altered disc tilting in our WAXS pattern, i.e., a splitting of the short-range order peaks characteristic of intracolumnar disc−disc stacking, we rather favor the chain freezing hypothesis. Nevertheless, we believe that a more thorough investigation of the bulk PCry phase of the present mesogen family would be important in the future to completely rule out a disc tilting contribution to the observed phenomenology.

Particularly noteworthy is also the observation of a confinement-induced nematic discotic phase in the case of Cy16, since such a phase has been barely found in other DILC systems in the bulk state.[3]

For the hydrophobic confinement, two orientational transitions can be inferred from the optical birefringence experiments for each mesogen; see Figure 4. However, for the most hydrophilic one (Cy12) no decrease in the optical retardation at lower temperatures is observed but rather an additional increase and thus increased radial orientation of the superdisc normals at low temperatures. By contrast, for the more hydrophobic molecules both the diffraction experiments (observation of two Bragg peaks) and decrease in optical retardation indicate the formation of axially oriented columns at low temperatures.

It is also interesting to mention that except for Cy14 no diffraction patterns (Bragg peaks) can be detected upon the first optical retardation increase. This means that in both cases only collective orientational order, but no translational columnar order, emerges upon cooling from the isotropic state. The systems form nematic discotic states.

Note that we indicate for Cy12 at low and Cy14 for intermediate temperatures a circular concentric columnar ring formation, in analogy to the analogous observation for classic discotic systems; see Figure 4e(i),(ii). This conclusion is drawn from the observation of a 6-fold pattern in combination with the boundary condition of an edge-on anchoring of the discs at the pore walls; see Figure 4f(i),(ii). Unfortunately, both the circular concentric ring formation as well as the logpile structures result effectively in the same qualitative Bragg ring distribution in reciprocal space, since both emerge from the rotation of a hexagon about the pore axis in reciprocal space.[23,50] Whereas for DLC, AFM studies could confirm this structure formation for edge-on anchoring, we can only indirectly infer this.[50] Also, reasoning with regard to correlation lengths did not provide a more conclusive result.

https://doi.org/10.1021/acsnano.4c01062
ACS Nano XXXX, XXX, XXX−XXX

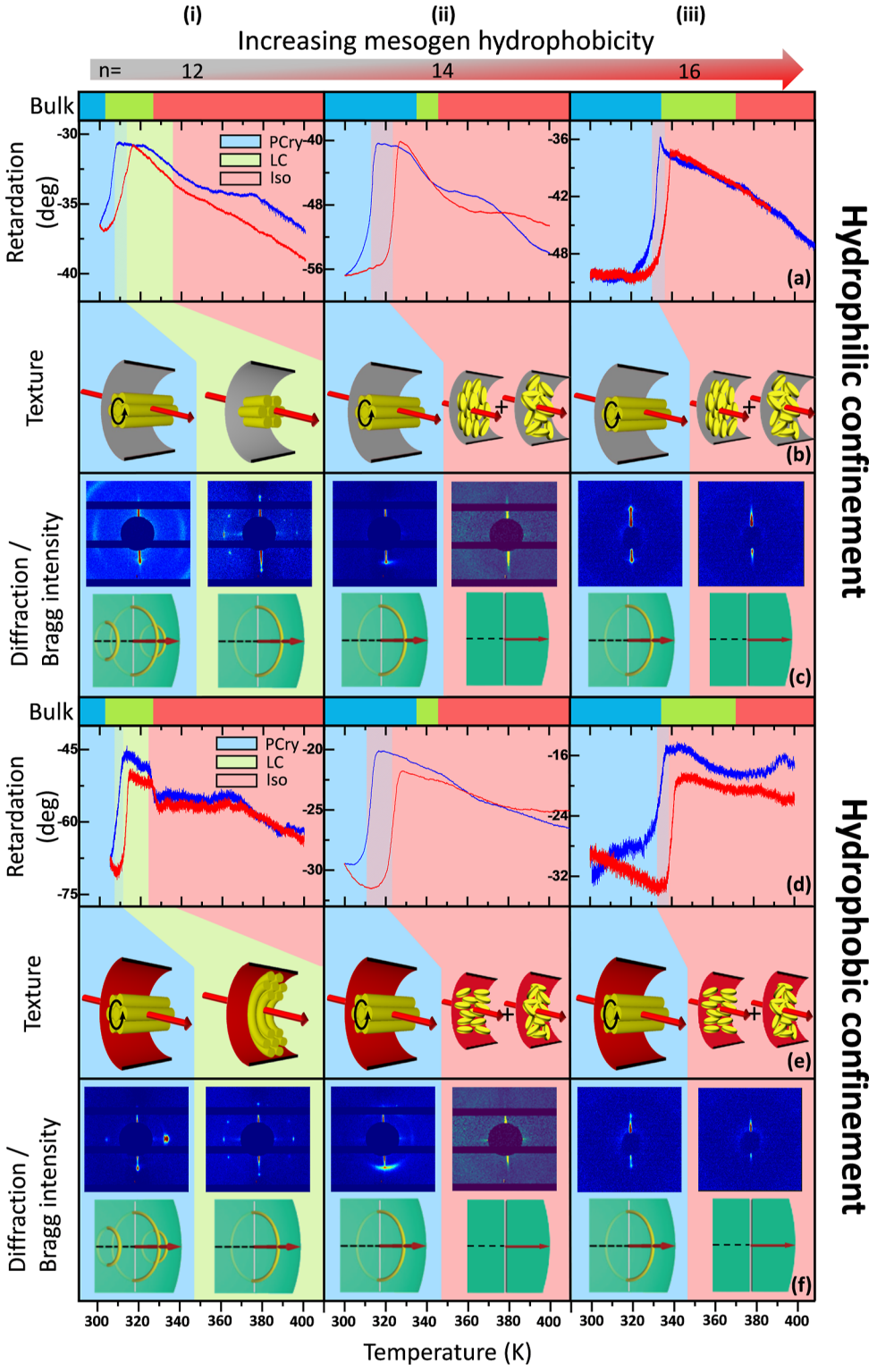

Figure 7. Self-assembly of acyclic Dopa-ILCs as a function of mesogen hydrophilicity in hydrophilic and hydrophobic nanochannels. Birefringence curves and XRD patterns of acyclic Dopa-ILC molecules with different side chain lengths confined in hydrophilic (native) and hydrophobic (ODPA-modified) nanopores with 180 nm pore size in different phases. The temperature ranges of the distinct bulk phases of each Dopa-ILC are given above its retardation curve. The measured SAXS patterns and schematics of the corresponding scattering geometry and Bragg intensities in reciprocal space intersecting the Ewald sphere in both the plastic crystalline and liquid crystalline phases are also given. The background color of the birefringence curves refers to different phases of the ILCs (blue: PCry phase, green: LC phase, red: Iso phase). The dashed areas at the phase transition refer to the hysteresis between the cooling and heating processes.

In summary, the cyclic Dopa-ILCs confined in 180 nm hydrophilic and hydrophobic pores show a clear dependence on the molecular hydrophobicity (side chain length). ILCs with shorter side chains and thus a dominance of the hydrophilic core tend to orient radially with uniform collective orientation and translational order in both the LC and PCry

https://doi.org/10.1021/acsnano.4c01062
ACS Nano XXXX, XXX, XXX−XXX

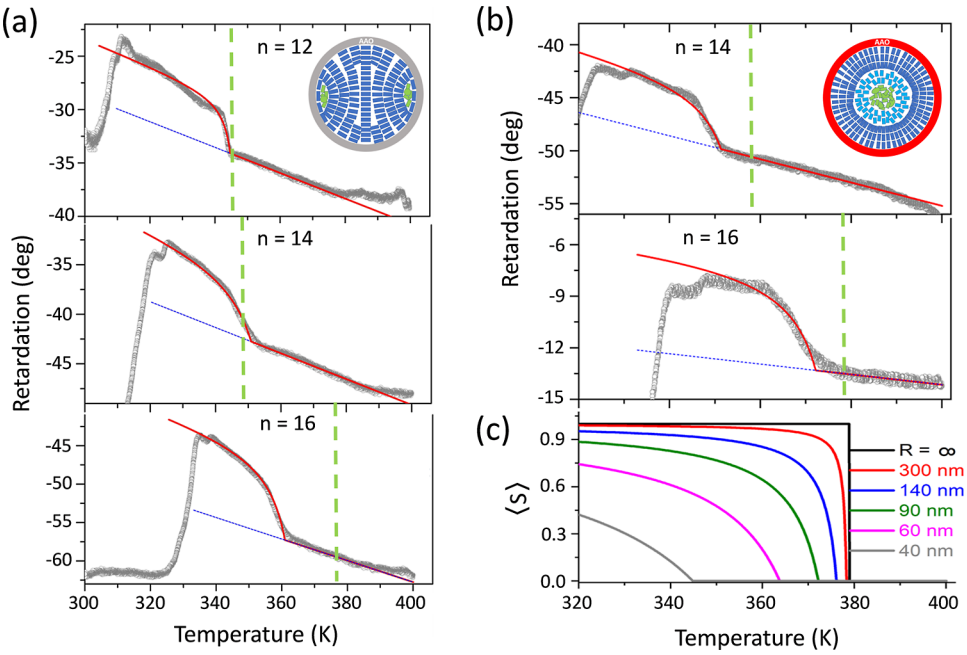

Figure 8. Landau-de-Gennes modeling of the cyclic Dopa-ILCs phase behavior in (a) hydrophilic and (b) hydrophobic nanopores. The green dashed line shows the first-order bulk phase transition temperature and the red curve shows the fitting curve using the Landau-de-Gennes theory. Inset: (a) logpile configuration of Dopa-ILCs in hydrophilic pores and (b) circular concentric configuration of Dopa-ILCs in hydrophobic pores. (c) Simulations on the dependence of effective orientational order parameter ⟨*S*⟩ of Dopa-ILCs confined in different pore sizes.

phases under confinement, whereas larger molecules with longer side chains tend to orient radially only in their LC phase. As the temperature decreases into the PCry phase, the larger molecules adopt an axial configuration instead to avoid high bending energy and spatial distortion due to the freezing of their long side chains. This emphasizes again the importance of the bending elasticity for the texture formation in nanoconfinement.

Translational and Collective Orientational Order of Acyclic Dopa-ILCs Confined in 180 nm AAO Membranes. In Figure 7 , we show the SAXS measurement of the Dopa-ILCs with acyclic imidazolium five-membered ring (acyclic Dopa-ILCs) confined in both hydrophilic and hydrophobic AAO membranes with 180 nm pore sizes. For the acyclic Dopa-ILC with the shortest side chain length $n = 12$ (Ac12) confined in both hydrophilic and hydrophobic pores as shown in Figure 7(i), 6-fold diffraction patterns are first observed in their LC phase. This indicates a logpile structure in hydrophilic pores and a circular concentric structure in hydrophobic pores, as already discussed in the previous section. If the sample is further cooled to the PCry phase, the 6-fold pattern evolves into a pair of equatorial peaks, which is the typical diffraction pattern for an axial structure. Therefore, when the Ac12 sample is cooled from the LC to the PCry phase, an interesting structural transition from a radial to axial structure is again observed. A similar conclusion can also be drawn from the birefringence curves as shown in Figure 7a(i),d(i). For both hydrophilic and hydrophobic membranes, the retardation value first increases on cooling from the isotropic phase to the LC phase, forming a logpile/circular concentric structure in the nanopores. Then, similarly, as for the cyclic DILCs on further cooling to the PCry phase, the side chains of the ILC molecules freeze, resulting in higher chain stiffness. An axial structure is energetically preferred to avoid the high bending and splay distortion of the logpile/circular concentric configuration. As a result, when cooled from the LC phase to the PCry phase, Ac12 shows a decrease in the retardation value caused by the radial to axial configuration transformation.

For the DILCs with acyclic functional groups, the molecular hydrophobicity increases with increasing alkyl side chain lengths. When confined in both hydrophilic and hydrophobic pores as shown in Figure 7(ii),(iii), both Ac14 and Ac16 first show no obvious diffraction pattern in the LC phase and then the polar peaks appear in the PCry phase, indicating no molecular translational order in the LC phase and an axial configuration in the PCry phase. The same conclusion can also be drawn from the birefringence curves, where the retardation values show no obvious boundaries between the isotropic phase and LC phase and a sharp decrease when cooled to the PCry phase.

Landau-de Gennes Analysis of the Isotropic-to-Liquid-Crystal Transitions. The optical retardation is a direct measure of the liquid crystalline order parameter ⟨*S*⟩. Whereas for the acyclic systems, barely any systematic thermotropic changes in the optical birefringence between the Iso and LC phases can be detected, for the cyclic systems quite pronounced changes in the retardation are visible. In all cases, it shows a continuous transition behavior in the region of the Iso to LC phase transition $T_{Iso \rightarrow LC}$, which contrasts with the discontinuous jump-like behavior of the order parameter characteristic of the first-order transition observed in the corresponding bulk systems, as seen in, for example, the evolution of the birefringence of a bulk film of Cy12, Cy14, and Cy16 in the Supporting information. This observation is also in agreement with the findings in our previous dielectric and calorimetric study.[55]

https://doi.org/10.1021/acsnano.4c01062
ACS Nano XXXX, XXX, XXX−XXX

In general, such a behavior can be rationalized by considering two mechanisms: (i) interfacial anchoring and (ii) inhomogeneous deformations of the director fields caused by cylindrical confinement, which dominate in different temperature regions, i.e., in the confined Iso and LC phases, respectively.

The molecular ordering due to the Iso-LC transition contributes to the excess birefringence and is linearly related to its optical retardation. It appears in the background of the temperature-dependent birefringence. As a reasonable approximation, the bare geometrical retardation is assumed to be linearly dependent on temperature, so in most analyses, its value is extrapolated from the parent phase, in this case, the isotropic one. The excess retardation can be positive or negative, depending on the optical molecular anisotropy and molecular arrangement. Our X-ray scattering experiments suggest a logpile face-on configuration for hydrophilic cylindrical channels and a circular concentric configuration for hydrophobic channels. Therefore, excess optical retardation is expected to be positive in both cases, which is consistent with the polarimetry measurements.

Homeotropic (or face-on) anchoring of discotic Dopa-ILC building blocks to the hydrophilic cylindrical walls of the host matrix occurs well above the $T_{\mathrm{Iso}\rightarrow\mathrm{LC}}$. As the temperature decreases, the anchoring effects strengthen as a result of the increase in the number of statistically anchored molecules at the pore walls in the confined isotropic phase. For rod-like nematic systems, this typically results in a pretransitional tail and in a paranematic state. It is associated with a geometrical ordering field, $\sigma \propto 1/R$, enforcing arrangement of rod-like molecules along the channel long axis.[31] Under increasing confinement, such nematogen systems reveal a crossover from discontinuous to continuous temperature evolution of their orientational (nematic) order parameter with a characteristic critical point.[31,52,59] This mechanism, however, is not fully applicable to discotic molecules homeotropically anchored on cylindrical pore walls: The optical polarizability of discotic molecules is isotropic in their aromatic plane; thus, any lateral rotation of them keeps the effective optical anisotropy of the LC composite unchanged despite the fact that face-on bonding indeed takes place giving a certain contribution to the optical retardation in the paranematic phase. Accordingly, there are no pretransitional tails observable. The linear increase in birefringence with temperature above the transition is traceable to the purely linear increase in geometric birefringence, see blue lines in Figure 8.

The most probable reason for a continuous evolution of the effective orientational order parameter $\langle S\rangle$, likewise related to its retardation ($R \propto \langle S\rangle$), is the inhomogeneous bend and splay deformation of the columns caused by cylindrical confinement. For face-on anchoring with logpile arrangement in the pore center, this is schematically shown in the inset of Figure 8a. Note that we emphasize in this drawing the distinct kinds of deformations for clarity. Besides that, in the small area between the columns and the pore wall there also exist some randomly distributed molecules. The splay/bend deformation as well as the small random area all introduce excess energy and contribute to the shift of the phase transition temperature. Unfortunately, the resulting inhomogeneous director field along with the unknown knowledge of the detailed relative contributions of splay and bend deformation along the nanochannel axis and in the cross section hamper a sound analytical treatment of the defect energy contributions. Interestingly, however, a fitting of the continuous behavior by a Landau-de Gennes excess free energy that solely considers the splay deformations at the walls already results in a very good agreement with the continuous evolution of the order parameter; see the fits in Figure 8a. A detailed description of the corresponding model is given in chapter III.E of ref 49.

Fortunately, edge-on anchoring, which is characteristic of hydrophobically grafted cylindrical AAO channel walls, leads to a theoretically more tractable director field in the case of circular concentric column formation. The formation of circular columns results in bending stresses, $|\vec{n} \times (\vec{\nabla} \times \vec{n})| = 1/r$, while the splay and twist distortions are both zero.[6,50] The biquadratic coupling between the orientational order parameter $\langle S\rangle$ and the bending distortion [$b_3(\vec{n} \times (\vec{\nabla} \times \vec{n}))^2 S^2$-term] causes a distinct, local transition temperature $T_c(r) = T'(R) - b_3 A^{-1} r^{-2}$ for each circular concentric ring with ring radius r. According to this formalism, circular concentric layers start to form near the channel walls during cooling at $T_{\mathrm{ICD}} = T'(R) - b_3 A^{-1} r^{-2} = T_{\mathrm{ICD}}{}^{\#} - g/R - b_3 A^{-1} R^{-2}$. The radius of the cylindrical phase front r_c separating the isotropic core from the circular columnar shell is defined as $r_c(T) = [b_3 A^{-1}/(T'(R) - T)]^{1/2}$, i.e. it gradually shrinks toward the channel center as it cools. However, it can be seen that even at $T \rightarrow 0$, $r_c(T = 0) = [b_3 A^{-1}/T'(R)]^{1/2}$: the radius of the isotropic core tends to a finite nonzero value. Therefore, it can be assumed that the circular concentric arrangement of discotic columns is characterized by gradual frustration as one moves from the periphery to the center of the channel, first losing columnar (positional) order, resulting in the formation of an intermediate bent nematic layer, and finally losing orientational order as one approaches the isotropic core; see sketch in inset of Figure 8b. Assuming fully saturated order in the subsequent circular columns and in the bent nematic layer, the effective order parameter in the relevant phase is defined as $\langle S(T)\rangle = 1 - b_3 A^{-1} R^{-2} (T'(R) - T)^{-1}$. Figure 8b shows the temperature dependence of the optical retardation $\Delta(T)$ (gray dots) measured on cooling (hydrophobic grafting); see Figure 7d and corresponding fits (red curves) for comparison. Moreover, Figure 8c shows simulated $\langle S(T)\rangle$ dependencies ($R = \infty$, 300, 140, 90, 60, and 40 nm). Such a bend distortion model reproduces the temperature dependence of the optical retardation close to the phase transition point well, in particular its rounded kink-like character. Note that this reasoning is also consistent with the conclusions regarding a DLC (HAT6) confined in hydrophobic silica nanopores.[6] Due to the large ratio of molecule size to pore diameter, the bending energy differences of the circular ring layers with distinct radii are even so large for this system that a layer-by-layer quantized transition behavior has been observed both in experiment and in Monte Carlo computer simulations.[6]

CONCLUSIONS

We presented temperature-dependent high-resolution optical birefringence measurements and 3D reciprocal space mappings based on synchrotron-based X-ray scattering to investigate the thermotropic phase behavior of dopamine-based ILCs in cylindrical channels of 180 nm diameter in AAO membranes. As a function of the hydrophilicity and thus the molecular anchoring to the pore walls (edge-on or face-on) and the variation of the hydrophilic−hydrophobic balance between the

https://doi.org/10.1021/acsnano.4c01062
ACS Nano XXXX, XXX, XXX−XXX

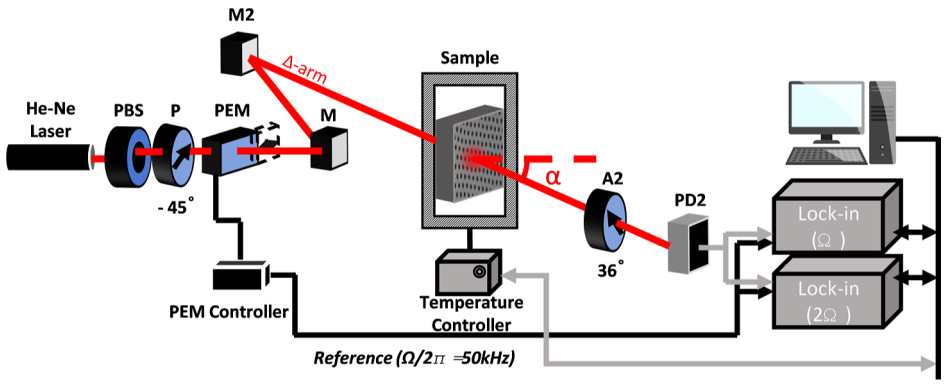

Figure 9. Sketch of the setup for birefringence measurements. PBS is the polarizing beam splitter, which splits the laser beam into a Ψ arm and a Δ arm. For birefringence measurement in this work, only the Δ arm is used. P refers to the polarizer. PEM is the Photon Elastic Modulator. M2 is the mirror and $\lambda/4$ is a quarter wave plate. The sample is placed in a sealed sample chamber with an argon atmosphere. A2 is the analyzer with its polarization direction perpendicular to the polarizer. PD2 is the photodiode that detects the modularized light and transfers the data to the corresponding lock-in amplifier for further analysis.

aromatic cores and the alkyl side chain motifs of the superdiscs, we find a particularly rich phase behavior, which is not present in the bulk state.

Comparing the cyclic and acyclic molecules with the same side chain length, it can be inferred that the acyclic five-membered ring as a functional group introduces a higher molecular hydrophobicity in comparison to the cyclic five-membered ring. For example, Cy14 still shows a radial structure, while Ac14 forms only a less ordered paranematic structure in its LC phases.

For both cyclic and acyclic Dopa-ILCs with different side chain lengths, it can be concluded from the birefringence curves and SAXS patterns that DILCs with lower molecular hydrophobicity (shorter side chain) tend to orient radially under cylindrical confinement, whereas DILCs with higher molecular hydrophobicity (longer side chain) tend to form a paranematic structure in the LC phase. Nematic phases of bulk DILCs are found rather rarely.

Also confinement-induced continuous order formation is observed in contrast to discontinuous first-order phase transitions, which can be quantitatively described by Landau-de Gennes free energy models for liquid crystalline order transitions in confinement.

Upon cooling from the LC phase to the PCry phase, presumably due to the freezing of the alkyl side chains and the consequent increase in molecular stiffness and hydrophobicity, almost all ILCs adopt an axial structure to avoid the high bending/splay energy resulting from the radial structure. Among them, Cy14 and Ac12 show particularly interesting structural behavior upon cooling from LC to PCry phase. Both give clear indications of the structural transition from logpile (hydrophilic) or circular concentric (hydrophobic) orientation to an axial orientation with decreasing temperature. Thus, the DILC system presented here is a fine example where a cooling-induced increase in the bending rigidity of discotic columns drives a textural transition from a radial to an axial self-assembly in nanoconfinement.

In terms of applications, the temperature- and confinement-dependent radial-to-axial phase transition as well as nematization could be very interesting for the design of nanoporous functional devices and membranes with tunable ionic conductivity along the tubular nanopores or for optical hybrids with tunable birefringence.

EXPERIMENTAL SECTION

Materials. The synthesis of the investigated DILCs is described in ref 10. Their multiscale self-assembly is illustrated in Figure 1. The single ILC molecular block is based on L-3,4-dihydroxyphen-ylalanine (Dopa-ILC). It consists of a large organic cation with an aromatic core (blue), three alkyl side chains, as well as a chloride counterion (green). Dopa-ILCs with two different functional groups as cationic units (cyclic or acyclic imidazolium five-membered ring) are investigated, and, in both cases, the chain lengths of the alkyl side chains are varied (n = 12, 14, and 16). A single Dopa-ILC molecule has a conical shape due to the presence of three flexible alkyl chains, resulting in inverted micellar-type self-assembled discs (Figure 1b), where each disc is composed of six Dopa-ILC mesogens.[10] Given the chemical structure of the disc units, each disc should be hydrophilic in the center and hydrophobic at the edge. Driven by the $\pi-\pi$ interactions between the aromatic cores, the discs can further self-organize and stack in columns, leading to a hexagonally ordered columnar liquid crystalline mesophase.[5]

Nanoporous AAO membranes purchased from SmartMembranes GmbH (Halle, Germany) were used as the host material to confine the Dopa-ILCs. The membranes are 1 × 1 cm square pieces with a thickness of 100 μm. Cylindrical pores with a pore diameter of 180 nm are hexagonally distributed on the membrane. The native AAO membranes have hydrophilic pore walls and, therefore, provide hydrophilic confinement. To investigate the influence of surface chemistry on the self-assembly behavior, the AAO membranes are also modified by chemical treatment with octadecylphosphonic acid (ODPA) to create a hydrophobic confinement environment.[60] During the ODPA treatment, hydrophilic O−H surface groups are replaced by hydrophobic P−O_3−$(CH_3)_{18}$ ones, resulting in hydrophobic pore surfaces.

Sample Preparation. DILCs are confined into nanoporous AAO membranes via spontaneous imbibition.[61] The membranes are first degassed at 200 °C for 20 h. They are then placed on top of DILCs at a temperature of 20 K above the bulk columnar-to-isotropic phase transition point of the corresponding liquid crystal for 48 h in an argon environment. The Laplace pressure causes spontaneous infiltration of the molten liquid crystals into the nanoporous membrane. After the pores are filled, the remaining bulk material on the surface of the membranes is carefully removed with a razor blade.

As shown in Figure 2, the native nanoporous AAO membranes are hydrophilic, which favors face-on (homeotropic) anchoring of the discs on the pore walls. After chemical modification with ODPA, the pore walls become hydrophobic, which favors edge-on (planar or homogeneous) anchoring of the discs. Although the chemical modification with ODPA grafts a layer of alkyl chains onto the pore walls, the liquid crystal molecules can push the alkyl chains toward the

https://doi.org/10.1021/acsnano.4c01062
ACS Nano XXXX, XXX, XXX−XXX

pore wall after full infiltration and the alkyl chains only form a 2.2 nm thick layer on the pore wall and, therefore, the pore sizes of the chemically modified membranes are considered to be unchanged compared to the native membranes.[23]

Optical Birefringence Measurement. Temperature-dependent optical birefringence measurements are performed to determine the collective thermotropic orientation of the discotic Dopa-ILC units in the nanopores.

The optical birefringence measurement setup uses a He−Ne laser (λ = 632.8 nm) as a linearly polarized light source. As shown in Figure 9, the laser beam first passes through a polarizer in order to be linearly polarized at an angle of 45° to the direction of propagation. The photoelastic modulator (PEM) is used to apply a time-modulated delay to the beam. The beam measuring the linear birefringence (δ-arm) is reflected by two mirrors and passes through the sample at an angle of incidence of α = 36°. The beam then passes through an analyzer set perpendicular to the polarizer and reaches the photodiode. Two SR830 lock-in amplifiers from Stanford Research Systems (Sunnyvale, USA) connected to the detector measure the amplitudes of the first and second harmonics using two reference signals that are locked at 50 and 100 kHz from the modulated light intensities. The corresponding optical retardation is calculated from the measured light intensities.

Throughout the measurement, the temperature of the sample is increased and decreased at a controlled rate (0.15 K/min) to observe the thermotropic effect. By measuring the optical retardation between the ordinary beam and the extraordinary beam, we obtain information about the collective orientation change of the molecules during heating and cooling in the nanopores. During cooling into the liquid crystalline phase, an increase in the retardation value indicates that the rotational axis of the discotic units is collectively perpendicular to the pore axis, while a decrease in the retardation value indicates that the rotational axis of the discotic units is collectively parallel to the pore axis.[62,63]

X-ray Scattering Experiments. To obtain detailed information about the molecular packing of the DILCs, temperature-dependent (1 K/min) X-ray scattering experiments in transmission were performed at the P08 beamline[64] of the PETRA III synchrotron at Deutsches Elektronen-Synchrotron DESY (beam size (V×H) = (200 × 200) μm^2, beam wavelength λ = 0.496 Å, PerkinElmer detector) and the BM02 beamline of the European Synchrotron Radiation Facility ESRF (beam size (V×H) = (55 × 55) μm^2, beam wavelength λ = 0.688 Å); see Figure 10 for a sketch of the scattering geometry and used naming conventions. The temperature-dependent X-ray scattering patterns are taken at ω = 85°, where the X-ray beam is almost perpendicular to the long axis of the pores, $\hat{p}$. Additional rotation scans are performed at selected temperatures for sample rotation angles from ω = 90 → 0°. For ω = 85° only order along $\hat{p}$ is probed, while ω = 0° probes dominantly order perpendicular to $\hat{p}$ since the scattering vector $\vec{q}$ is nearly perpendicular to the beam direction at small scattering angles. Similar to fiber diffraction, we define the χ = 0° axis as the polar direction and the χ = 90° axis as the equatorial direction since we consider the long pore axis as equivalent to the fiber direction.[23,50] By performing Gaussian line shape fits to the scattering profiles, the full width at half-maximum (fwhm) is extracted and in turn enables a calculation of the average domain sizes through the Scherrer equation. Here, the domain size is described as $\chi = K \cdot \lambda / \Delta\theta \cdot \cos(\theta)$, where λ is the wavelength, θ is the Bragg angle, $\Delta\theta$ is the fit obtained fwhm, and K = 0.9 is an empirical proportionality factor. Using this approach, both the coherence lengths along the pore axis ($\chi_{\parallel}$) and perpendicular to the pore axis ($\chi_{\perp}$) are determined.

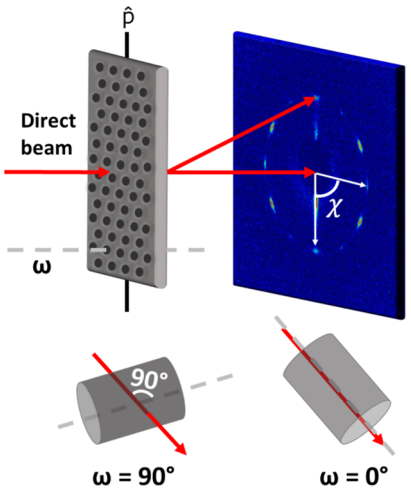

Figure 10. Schematics of the synchrotron-based X-ray scattering experiment. Shown are configurations with the long pore axis direction $\hat{p}$ perpendicular and parallel to the incident (direct) beam, which corresponds to sample rotation angles ω = 90 and ω = 0°, respectively. Also indicated is the definition of the azimuth angle χ.

ASSOCIATED CONTENT

Supporting Information

The Supporting Information is available free of charge at https://pubs.acs.org/doi/10.1021/acsnano.4c01062.

Experimental procedures and characterization data for all compounds are provided in the supporting information (ZIP)

Self-assembly of ionic superdiscs in nanopores (PDF)

AUTHOR INFORMATION

Corresponding Author

Patrick Huber − *Institute for Materials and X-ray Physics, Hamburg University of Technology, 21073 Hamburg, Germany; Centre for X-ray and Nano Science CXNS, Deutsches Elektronen-Synchrotron DESY, 22607 Hamburg, Germany;* orcid.org/0000-0002-2126-9100; Email: patrick.huber@tuhh.de

Authors

Zhuoqing Li − *Institute for Materials and X-ray Physics, Hamburg University of Technology, 21073 Hamburg, Germany; Centre for X-ray and Nano Science CXNS, Deutsches Elektronen-Synchrotron DESY, 22607 Hamburg, Germany*

Aileen Raab − *Institut für Organische Chemie, Universität Stuttgart, 70569 Stuttgart, Germany;* orcid.org/0000-0003-4591-1513

Mohamed Aejaz Kolmangadi − *Bundesanstalt für Materialforschung und -prüfung (BAM), 12205 Berlin, Germany;* orcid.org/0000-0002-5574-3165

Mark Busch − *Institute for Materials and X-ray Physics, Hamburg University of Technology, 21073 Hamburg, Germany; Centre for X-ray and Nano Science CXNS, Deutsches Elektronen-Synchrotron DESY, 22607 Hamburg, Germany*

Marco Grunwald − *Institut für Organische Chemie, Universität Stuttgart, 70569 Stuttgart, Germany*

Felix Demel − *Institut für Organische Chemie, Universität Stuttgart, 70569 Stuttgart, Germany*

Florian Bertram − *Deutsches Elektronen-Synchrotron DESY, 22607 Hamburg, Germany*

Andriy V. Kityk − *Faculty of Electrical Engineering, Czestochowa University of Technology, 42-200 Czestochowa, Poland;* orcid.org/0000-0002-4823-3220

https://doi.org/10.1021/acsnano.4c01062
ACS Nano XXXX, XXX, XXX−XXX

Andreas Schönhals − *Bundesanstalt für Materialforschung und -prüfung (BAM), 12205 Berlin, Germany; Institut für Chemie, Technische Universität Berlin, 10623 Berlin, Germany;* orcid.org/0000-0003-4330-9107

Sabine Laschat − *Institut für Organische Chemie, Universität Stuttgart, 70569 Stuttgart, Germany;* orcid.org/0000-0002-1488-3903

Complete contact information is available at: https://pubs.acs.org/10.1021/acsnano.4c01062

Notes

The authors declare no competing financial interest.

A submitted version of this publication has been stored on Arxiv.org;[65] see (10.48550/arXiv.2401.12663).

ACKNOWLEDGMENTS

Funding by the Deutsche Forschungsgemeinschaft (DFG, German Research Foundation) within the project "Ionic Liquid Crystals Confined in Nanoporous Solids: Self-Assembly, Molecular Mobility and Electro-Optical Functionalities", Projektnummer 430146019, as well as the collaborative research center CRC 986 "Tailor-Made Multi-Scale Materials Systems", Projektnummer 192346071, is acknowledged. We thank Deutsche Elektronen-Synchrotron DESY, Hamburg, for access to the beamline P08 of the PETRA III synchrotron. We also acknowledge the European Synchrotron Radiation Facility (ESRF) for provision of synchrotron radiation facilities and we thank Gilbert Chahine and Isabelle Morfin for assistance and support in using beamline BM02. The presented results are part of a project that has received funding from the European Union's Horizon Europe research and innovation programme under the Marie Skłodowska-Curie Grant agreement no. 101086493. A.V.K. acknowledges the project cofinanced by the Polish Ministry of Education and Science under the program "Co-financed international projects", project no. W26/HE/2023 (Dec. MEN 5451/HE/2023/2).

REFERENCES

(1) Goossens, K.; Lava, K.; Bielawski, C. W.; Binnemans, K. Ionic Liquid Crystals: Versatile Materials. *Chem. Rev.* **2016**, *116*, 4643−4807.

(2) Devaki, S. J.; Sasi, R. Ionic Liquids/Ionic Liquid Crystals for Safe and Sustainable Energy Storage Systems. *IntechOpen.* **2017**, 14.

(3) Kapernaum, N.; Lange, A.; Ebert, M.; Grunwald, M. A.; Haege, C.; Marino, S.; Zens, A.; Taubert, A.; Giesselmann, F.; Laschat, S. Current Topics in Ionic Liquid Crystals. *ChemPlusChem* **2022**, *87*, No. e202100397.

(4) Axenov, K. V.; Laschat, S. Thermotropic Ionic Liquid Crystals. *Materials* **2011**, *4*, 206−259.

(5) Yildirim, A.; Szymoniak, P.; Sentker, K.; Butschies, M.; Bühlmeyer, A.; Huber, P.; Laschat, S.; Schönhals, A. Dynamics and ionic conductivity of ionic liquid crystals forming a hexagonal columnar mesophase. *Phys. Chem. Chem. Phys.* **2018**, *20*, 5626−5635.

(6) Sentker, K.; Zantop, A. W.; Lippmann, M.; Hofmann, T.; Seeck, O. H.; Kityk, A. V.; Yildirim, A.; Schönhals, A.; Mazza, M. G.; Huber, P. Quantized Self-Assembly of Discotic Rings in a Liquid Crystal Confined in Nanopores. *Phys. Rev. Lett.* **2018**, *120*, 067801.

(7) Bisoyi, H. K.; Li, Q. Liquid Crystals: Versatile Self-Organized Smart Soft Materials. *Chem. Rev.* **2022**, *122*, 4887−4926.

(8) Kato, T.; Yoshio, M.; Ichikawa, T.; Soberats, B.; Ohno, H.; Funahashi, M. Transport of ions and electrons in nanostructured liquid crystals. *Nat. Rev. Mater.* **2017**, *2*, 17001.

(9) Salikolimi, K.; Sudhakar, A. A.; Ishida, Y. Functional Ionic Liquid Crystals. *Langmuir* **2020**, *36*, 11702−11731.

(10) Neidhardt, M. M.; Schmitt, K.; Baro, A.; Schneider, C.; Bilitewski, U.; Laschat, S. Self-assembly and biological activities of ionic liquid crystals derived from aromatic amino acids. *Phys. Chem. Chem. Phys.* **2018**, *20*, 20371−20381.

(11) Kawata, K. Orientation Control and Fixation of Discotic Liquid Crystal. *Chem. Rec.* **2002**, *2*, 59−80.

(12) Eichhorn, S. H.; Adavelli, A.; Li, H. S.; Fox, N. Alignment of Discotic Liquid Crystals. *Mol. Cryst. Liq. Cryst.* **2003**, *397*, 47−58.

(13) Lugger, J. A. M.; Mulder, D. J.; Bhattacharjee, S.; Sijbesma, R. P. Homeotropic Self-Alignment of Discotic Liquid Crystals for Nanoporous Polymer Films. *ACS Nano* **2018**, *12*, 6714−6724.

(14) Pipertzis, A.; Zardalidis, G.; Wunderlich, K.; Klapper, M.; Müllen, K.; Floudas, G. Ionic Conduction in Poly(ethylene glycol)-Functionalized Hexa-peri-hexabenzocoronene Amphiphiles. *Macromolecules* **2017**, *50*, 1981−1990.

(15) Wöhrle, T.; Wurzbach, I.; Kirres, J.; Kostidou, A.; Kapernaum, N.; Litterscheidt, J.; Haenle, J. C.; Staffeld, P.; Baro, A.; Giesselmann, F.; Laschat, S. Discotic Liquid Crystals. *Chem. Rev.* **2016**, *116*, 1139−1241.

(16) Cleaver, D. J.; Kralj, S.; Sluckin, T. J.; Allen, M. P. Liquid crystals in complex geometries formed by polymer and porous networks. In *The random anisotropy nematic spin model*; Crawford, G. P., Zumer, S., Eds.; Taylor & Francis, 1996; pp 467−481.

(17) Matthias, H.; Röder, T.; Wehrspohn, R. B.; Kitzerow, H.-S.; Matthias, S.; Picken, S. J. Spatially periodic liquid crystal director field appearing in a photonic crystal template. *Appl. Phys. Lett.* **2005**, *87*, 241105.

(18) Kityk, A. V.; Huber, P. Thermotropic nematic and smectic order in silica glass nanochannels. *Appl. Phys. Lett.* **2010**, *97*, 153124.

(19) Chahine, G.; Kityk, A. V.; Demarest, N.; Jean, F.; Knorr, K.; Huber, P.; Lefort, R.; Zanotti, J.-M.; Morineau, D. Collective molecular reorientation of a calamitic liquid crystal (12CB) confined in alumina nanochannels. *Phys. Rev. E* **2010**, *82*, 011706.

(20) Ryu, S. H.; Gim, M.-J.; Lee, W.; Choi, S.-W.; Yoon, D. K. Switchable Photonic Crystals Using One-Dimensional Confined Liquid Crystals for Photonic Device Application. *ACS Appl. Mater. Interfaces* **2017**, *9*, 3186−3191.

(21) Spengler, M.; Dong, R. Y.; Michal, C. A.; Hamad, W. Y.; MacLachlan, M. J.; Giese, M. Hydrogen-Bonded Liquid Crystals in Confined Spaces-Toward Photonic Hybrid Materials. *Adv. Funct. Mater.* **2018**, *28*, 1800207.

(22) Bisoyi, H. K.; Li, Q. Stimuli directed alignment of self-organized one-dimensional semiconducting columnar liquid crystal nanostructures for organic electronics. *Prog. Mater. Sci.* **2019**, *104*, 1−52.

(23) Sentker, K.; Yildirim, A.; Lippmann, M.; Zantop, A. W.; Bertram, F.; Hofmann, T.; Seeck, O. H.; Kityk, A. V.; Mazza, M. G.; Schönhals, A.; Huber, P. Self-assembly of liquid crystals in nanoporous solids for adaptive photonic metamaterials. *Nanoscale* **2019**, *11*, 23304−23317.

(24) Sentker, K. Liquid Crystals in Nanoporous Solids: From Nanoscale Physics to Designing Metamaterials. Ph.D. thesis, Hamburg University of Technology, 2019.

(25) Huber, P.; Knorr, K. Adsorption-desorption isotherms and x-ray diffraction of Ar condensed into a porous glass matrix. *Phys. Rev. B* **1999**, *60*, 12657−12665.

(26) Alvine, K. J.; Pontoni, D.; Shpyrko, O. G.; Pershan, P. S.; Cookson, D. J.; Shin, K.; Russell, T. P.; Brunnbauer, M.; Stellacci, F.; Gang, O. Solvent mediated assembly of nanoparticles confined in mesoporous alumina. *Phys. Rev. B* **2006**, *73*, 125412.

(27) Alba-Simionesco, C.; Coasne, B.; Dosseh, G.; Dudziak, G.; Gubbins, K. E.; Radhakrishnan, R.; Sliwinska-Bartkowiak, M. Effects of confinement on freezing and melting. *J. Phys.: Condens. Matter* **2006**, *18*, R15−R68.

(28) Schaefer, C.; Hofmann, T.; Wallacher, D.; Huber, P.; Knorr, K. Melting and freezing of argon in a granular packing of linear mesopore arrays. *Phys. Rev. Lett.* **2008**, *100*, 175701.

(29) Huber, P. Soft matter in hard confinement: phase transition thermodynamics, structure, texture, diffusion and flow in nanoporous media. *J. Phys.: Condens. Matter* **2015**, *27*, 103102.
(30) Ocko, B. M.; Braslau, A.; Pershan, P. S.; Alsnielsen, J.; Deutsch, M. Quantized layer growth at liquid-crystal surfaces. *Phys. Rev. Lett.* **1986**, *57*, 94−97.
(31) Kutnjak, Z.; Kralj, S.; Lahajnar, G.; Zumer, S. Calorimetric study of octylcyanobiphenyl liquid crystal confined to a controlled-pore glass. *Phys. Rev. E* **2003**, *68*, 021705.
(32) Binder, K.; Horbach, J.; Vink, R.; De Virgiliis, A. Confinement effects on phase behavior of soft matter systems. *Soft Matter* **2008**, *4*, 1555−1568.
(33) Mazza, M. G.; Greschek, M.; Valiullin, R.; Kärger, J.; Schoen, M. Entropy-Driven Enhanced Self-Diffusion in Confined Reentrant Supernematics. *Phys. Rev. Lett.* **2010**, *105*, 227802.
(34) Araki, T.; Buscaglia, M.; Bellini, T.; Tanaka, H. Memory and topological frustration in nematic liquid crystals confined in porous materials. *Nat. Mater.* **2011**, *10*, 303−309.
(35) Çetinkaya, M. C.; Yildiz, S.; Özbek, H.; Losada-Pérez, P.; Leys, J.; Thoen, J. High-resolution birefringence investigation of octylcyanobiphenyl (8CB): An upper bound on the discontinuity at the smectic to nematic phase transition. *Phys. Rev. E* **2013**, *88*, 042502.
(36) Calus, S.; Kityk, A. V.; Eich, M.; Huber, P. Inhomogeneous Relaxation Dynamics and Phase Behaviour of a Liquid Crystal Confined in a Nanoporous Solid. *Soft Matter* **2015**, *11*, 3176−3187.
(37) Schlotthauer, S.; Skutnik, R. A.; Stieger, T.; Schoen, M. Defect topologies in chiral liquid crystals confined to mesoscopic channels. *J. Chem. Phys.* **2015**, *142*, 194704.
(38) Ryu, S. H.; Yoon, D. K. Liquid crystal phases in confined geometries. *Liq. Cryst.* **2016**, *43*, 1951−1972.
(39) Busch, M.; Kityk, A. V.; Piecek, W.; Hofmann, T.; Wallacher, D.; Całus, S.; Kula, P.; Steinhart, M.; Eich, M.; Huber, P. A ferroelectric liquid crystal confined in cylindrical nanopores: reversible smectic layer buckling, enhanced light rotation and extremely fast electro-optically active Goldstone excitations. *Nanoscale* **2017**, *9*, 19086−19099.
(40) Tran, L.; Lavrentovich, M. O.; Durey, G.; Darmon, A.; Haase, M. F.; Li, N.; Lee, D.; Stebe, K. J.; Kamien, R. D.; Lopez-Leon, T. Change in stripes for cholesteric shells via anchoring in moderation. *Phys. Rev. X* **2017**, *7*, 041029.
(41) Brumby, P. E.; Wensink, H. H.; Haslam, A. J.; Jackson, G. Structure and Interfacial Tension of a Hard-Rod Fluid in Planar Confinement. *Langmuir* **2017**, *33*, 11754−11770.
(42) Zhang, Y.-F.; Zhang, N.; Hingorani, H.; Ding, N.; Wang, D.; Yuan, C.; Zhang, B.; Gu, G.; Ge, Q. Fast-Response, Stiffness-Tunable Soft Actuator by Hybrid Multimaterial 3D Printing. *Adv. Funct. Mater.* **2019**, *29*, 1806698.
(43) Gang, O.; Huber, P.; Karim, A.; Zvonkina, I.; Lee, S.-W.; Kim, J.-W.; Roper, D. K.; Li, W. J. *Soft Matter and Biomaterials on the Nanoscale: The Wspc Reference on Functional Nanomaterials-Part I*; World Scientific, 2020; Vol. *1*.
(44) Monderkamp, P. A.; Wittmann, R.; Cortes, L. B. G.; Aarts, D. G. A. L.; Smallenburg, F.; Löwen, H. Topology of Orientational Defects in Confined Smectic Liquid Crystals. *Phys. Rev. Lett.* **2021**, *127*, 198001.
(45) Salgado-Blanco, D.; Llanas-García, A. H.; Díaz-Herrera, E.; Martínez-González, J. A.; Mendoza, C. I. Structural properties and ring defect formation in discotic liquid crystal nanodroplets. *J. Phys.: Condens. Matter* **2022**, *34*, 254001.
(46) Kopitzke, J.; Wendorff, J. H.; Glusen, B. Columnar discotics in confined geometries. *Liq. Cryst.* **2000**, *27*, 643−648.
(47) Duran, H.; Hartmann-Azanza, B.; Steinhart, M.; Gehrig, D.; Laquai, F.; Feng, X.; Müllen, K.; Butt, H.-J.; Floudas, G. Arrays of Aligned Supramolecular Wires by Macroscopic Orientation of Columnar Discotic Mesophases. *ACS Nano* **2012**, *6*, 9359−9365.
(48) Cerclier, C. V.; Ndao, M.; Busselez, R.; Lefort, R.; Grelet, E.; Huber, P.; Kityk, A. V.; Noirez, L.; Schönhals, A.; Morineau, D. Structure and Phase Behavior of a Discotic Columnar Liquid Crystal Confined in Nanochannels. *J. Phys. Chem. C* **2012**, *116*, 18990−18998.
(49) Kityk, A. V.; Busch, M.; Rau, D.; Calus, S.; Cerclier, C. V.; Lefort, R.; Morineau, D.; Grelet, E.; Krause, C.; Schönhals, A.; Frick, B.; Huber, P. Thermotropic orientational order of discotic liquid crystals in nanochannels: an optical polarimetry study and a Landau-de Gennes analysis. *Soft Matter* **2014**, *10*, 4522−4534.
(50) Zhang, R.; Zeng, X.; Prehm, M.; Liu, F.; Grimm, S.; Geuss, M.; Steinhart, M.; Tschierske, C.; Ungar, G. Honeycombs in Honeycombs: Complex Liquid Crystal Alumina Composite Mesostructures. *ACS Nano* **2014**, *8*, 4500−4509.
(51) Zhang, R.; Zeng, X.; Kim, B.; Bushby, R. J.; Shin, K.; Baker, P. J.; Percec, V.; Leowanawat, P.; Ungar, G. Columnar Liquid Crystals in Cylindrical Nanoconfinement. *ACS Nano* **2015**, *9*, 1759−1766.
(52) Całus, S.; Jabłońska, B.; Busch, M.; Rau, D.; Huber, P.; Kityk, A. V. Paranematic-to-nematic ordering of a binary mixture of rodlike liquid crystals confined in cylindrical nanochannels. *Phys. Rev. E* **2014**, *89*, 062501.
(53) Zhang, R.-B.; Ungar, G.; Zeng, X.; Shen, Z. Diverse configurations of columnar liquid crystals in cylindrical nano- and micropores. *Soft Matter* **2017**, *13*, 4122−4131.
(54) Yildirim, A.; Sentker, K.; Smales, G. J.; Pauw, B. R.; Huber, P.; Schönhals, A. Collective orientational order and phase behavior of a discotic liquid crystal under nanoscale confinement. *Nanoscale Adv.* **2019**, *1*, 1104−1116.
(55) Kolmangadi, M. A.; Zhuoqing, L.; Smales, G. J.; Pauw, B. R.; Wuckert, E.; Raab, A.; Laschat, S.; Huber, P.; Schönhals, A. Confinement-Suppressed Phase Transition and Dynamic Self-Assembly of Ionic Superdiscs in Ordered Nanochannels: Implications for Nanoscale Applications. *ACS Appl. Nano Mater.* **2023**, *6*, 15673−15684.
(56) Butschies, M.; Sauer, S.; Kessler, E.; Siehl, H. U.; Claasen, B.; Fischer, P.; Frey, W.; Laschat, S. Influence of N-Alkyl Substituents and Counterions on the Structural and Mesomorphic Properties of Guanidinium Salts: Experiment and Quantum Chemical Calculations. *ChemPhysChem* **2010**, *11*, 3752−3765.
(57) Kolmangadi, M. A.; Yildirim, A.; Sentker, K.; Butschies, M.; Bühlmeyer, A.; Huber, P.; Laschat, S.; Schönhals, A. Molecular dynamics and electrical conductivity of Guanidinium based ionic liquid crystals: Influence of cation headgroup configuration. *J. Mol. Liq.* **2021**, *330*, 115666.
(58) Grigoriadis, C.; Haase, N.; Butt, H.-J.; Müllen, K.; Floudas, G. Negative thermal expansion in discotic liquid crystals of nanographenes. *Adv. Mater.* **2010**, *22*, 1403−1406.
(59) Całus, S.; Rau, D.; Huber, P.; Kityk, A. V. Influence of nanoconfinement on the nematic behavior of liquid crystals. *Phys. Rev. E* **2012**, *86*, 021701.
(60) Grigoriadis, C.; Duran, H.; Steinhart, M.; Kappl, M.; Butt, H. J.; Floudas, G. Suppression of Phase Transitions in a Confined Rodlike Liquid Crystal. *ACS Nano* **2011**, *5*, 9208−9215.
(61) Gruener, S.; Huber, P. Imbibition in mesoporous silica: rheological concepts and experiments on water and a liquid crystal. *J. Phys.: Condens. Matter* **2011**, *23*, 184109.
(62) Kityk, A. V.; Wolff, M.; Knorr, K.; Morineau, D.; Lefort, R.; Huber, P.; Huber, P. Continuous paranematic-to-nematic ordering transitions of liquid crystals in tubular silica nanochannels. *Phys. Rev. Lett.* **2008**, *101*, 187801.
(63) Kityk, A. V.; Knorr, K.; Huber, P. Liquid n-hexane condensed in silica nanochannels: A combined optical birefringence and vapor sorption isotherm study. *Phys. Rev. B* **2009**, *80*, 035421.
(64) Seeck, O. H.; Deiter, C.; Pflaum, K.; Bertam, F.; Beerlink, A.; Franz, H.; Horbach, J.; Schulte-Schrepping, H.; Murphy, B. M.; Greve, M.; Magnussen, O. The high-resolution diffraction beamline P08 at PETRA III. *J. Synchrotron Radiat.* **2012**, *19*, 30−38.
(65) Li, Z.; Raab, A. R.; Kolmangadi, M. A.; Busch, M.; Grunwald, M.; Demel, F.; Bertram, F.; Kityk, A. V.; Schoenhals, A.; Laschat, S.; Huber, P. How do ionic superdiscs self-assemble in nanopores? **2024**, 2401.12663, arXiv. 10.48550/arXiv.2401.12663 (Jan 23, 2024).

https://doi.org/10.1021/acsnano.4c01062
ACS Nano XXXX, XXX, XXX−XXX